Phase-Field Model of Electronic Antidoping

Yin Shi,[1,*] Guo-Dong Zhao,[1] Ismaila Dabo,[1] Shriram Ramanathan,[2] and Long-Qing Chen[1,†]
[1]Department of Materials Science and Engineering, Pennsylvania State University, University Park, Pennsylvania 16802, USA
[2]Department of Electrical and Computer Engineering, Rutgers, The State University of New Jersey, Piscataway, New Jersey 08854, USA

(Received 15 February 2024; accepted 21 May 2024; published 18 June 2024; corrected 21 August 2024)

Charge carrier doping usually reduces the resistance of a semiconductor or insulator, but was recently found to dramatically enhance the resistance in certain series of materials. This remarkable antidoping effect has been leveraged to realize synaptic memory trees in nanoscale hydrogenated perovskite nickelates, opening a new direction for neuromorphic computing. To understand these phenomena, we formulate a physical phase-field model of the antidoping effect based on its microscopic mechanism and simulate the voltage-driven resistance change in the prototypical system of hydrogenated perovskite nickelates. Remarkably, the simulations using this model, containing only one adjustable parameter whose magnitude is justified by first-principles calculations, quantitatively reproduce the experimentally observed treelike resistance states, which are shown unambiguously to arise from proton redistribution-induced local band gap enhancement and carrier blockage. Our work lays the foundation for modeling the antidoping phenomenon in strongly correlated materials at the mesoscale, which can provide guidance to the design of novel antidoping-physics-based devices.

DOI: 10.1103/PhysRevLett.132.256502

In band semiconductors such as silicon, the electronic structure is rigid against charge carrier doping, which only shifts the Fermi energy toward the conduction or valence band edge, thereby increasing the carrier density and conductivity. In half-filled Mott insulators, charge carrier doping can not only shift the Fermi energy but also induce an insulator-to-metal transition [1], thus increasing the conductivity. However, it was recently found that carrier doping can cause a colossal *decrease* in the conductivity in several classes of solid-state materials that possess within the Mott-Hubbard gap additional intermediate bands that have been split from the principal conduction or valence band [2–6]. Examples of these materials are perovskite rare earth nickelates [2,7–15], $SrCoO_{3-\delta}$ [3], $Li_{\delta}FeSiO_4$ [4], $Li_{\delta}IrO_3$ [4], and $TiO_{2-\delta}$ [5]. This novel behavior poses a formidable challenge in understanding doping physics. It is worth pointing out that semiconductors typically find use after we understand how to dope them as seen in numerous examples over the years from silicon to gallium nitride. The microscopic theory derived from first-principles calculations illustrates that carriers doped onto the intermediate bands merge the occupied portion of the intermediate bands into the valence or conduction band, thereby exposing the large Mott-Hubbard gap and dramatically reducing the number of charge carriers (Fig. 1) [4,5,16].

This antidoping effect opens a new way of manipulating band gaps and resistance states, possibly giving rise to many novel applications. One outstanding example is perovskite rare earth nickelates. Hydrogen doping the nickelate $SmNiO_3$ enhances its resistivity by up to 8 orders of magnitude [2], enabling voltage-controlled tree-shaped resistance states [17]. This allows the emulation of neural trees [17] and synaptic networks [18], which has promising applications in adaptive computing. While simple models based on the phenomenologically exponential variation of resistance with doping concentration have been proposed to explain the nonlinear dependence of resistance on voltage bias [17,19], there is no theory yet to capture the treelike memory states and branching phenomena. Developing theoretical treatments of the evolution of electrical transport behavior is broadly relevant to understanding the physical properties of such quantum materials and is of increasing interest to beyond-von Neumann computing frameworks,

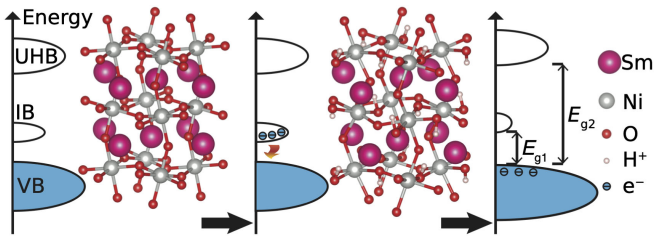

FIG. 1. Schematic diagrams of the density of electronic states showing the mechanism of antidoping. Electrons from hydrogen atoms are doped onto the intermediate band (IB), and then merge their occupied states into the valence band (VB), which may also enhance the gap (E_{g1}) across the valence band and the intermediate band and that (E_{g2}) across the valence band and the upper Hubbard band (UHB).

wherein materials with tunable band structures are highly sought after.

In this work, we develop a physical phase-field model of the antidoping effect based on its microscopic mechanism. We take the hydrogenated $SmNiO_3$ as a model example to investigate the antidoping-induced resistance states. Since the antidoping phenomenon is observed across this family of perovskite rare earth nickelates (e.g., $SmNiO_3$, $NdNiO_3$, $EuNiO_3$, etc.) [7,14,15], our theoretical treatment should be generalizable to other materials. The simulations quantitatively reproduce the experimentally observed treelike resistance states and demonstrate that a higher electric field reactivates the otherwise saturated proton distribution, which enhances the local band gap and carrier blockage, thereby generating a new resistance branch.

Inspired by the phase-field model of another strongly correlated material, vanadium dioxide [20,21], we write the chemical free energy density of nickelates as a sum of the intrinsic, correlated part f_L and the free carrier part $f_e - f_{e0}$,

$$F = \int [f_L(\eta, S_1, S_2) + f_e(\eta, p, n_1, n_2, n_H) - f_{e0}(\eta)]\mathrm{d}^d x, \quad (1)$$

where d is the spatial dimension and $\mathbf{x}$ is the spatial coordinate vector. η, S_1, and S_2 are the order parameters, p the free electron-hole density, n_1 the free electron density of the intermediate (ligand hole) band inside the Mott-Hubbard gap, n_2 the free electron density of the upper Hubbard band, and n_H the proton concentration. They are all fields dependent on $\mathbf{x}$ and time t. η characterizes the lattice structure and electronic phases ($\eta = 0$: orthorhombic metal; $\eta \neq 0$: monoclinic insulator), and S_1 and S_2 characterize the magnetic order ($S_1 = S_2 = 0$: paramagnetic; $S_1 \neq 0$ or $S_2 \neq 0$: antiferromagnetic) [22]. $f_L = f_{L0}(\eta, S_1, S_2) + \kappa_1(\nabla\eta)^2/2 + \kappa_2[(\nabla S_1)^2 + (\nabla S_2)^2]/2$, where f_{L0} is the local Landau potential energy density [22] and the other terms are the gradient or exchange energy density with κ_1 and κ_2 being constants. f_{L0} reproduces the temperature-tolerance factor phase diagram of the nickelates [22]. f_{e0} is f_e without doping so that $F = \int f_L \mathrm{d}^d x$ without doping at equilibrium.

To incorporate the antidoping effect into the free energy density of free carriers f_e, we consider the microscopic mechanism [4,5,16] in which the electrons released from the hydrogen atoms go to the intermediate band and are localized near the protons, thereby effectively consuming the itinerant states on the intermediate band (Fig. 1). The number of consumed itinerant states per unit volume should thus be equal to n_H. Because of the screening and drag of the localized electrons, the proton responds to electric fields with an effective charge q less than its nominal charge e, which is the amount of elementary charge. A characteristic of the insulator-metal transition is that the gap between the intermediate band and the valence band, E_{g1}, and that between the upper Hubbard band and the valence band, E_{g2}, both depend on the electronic phase order parameter η. The lowest order invariant approximations for the gaps are $E_{g1} = \Delta_1\eta^2$ and $E_{g2} = \Delta_2\eta^2$, where Δ_1 and Δ_2 are constants. By adopting the zero-band-width limit and setting the zero energy point to the midpoint between the valence and intermediate bands, we write f_e as

$$\begin{aligned} f_e = {} & \frac{\Delta_1\eta^2}{2}(p + n_1) + \left(\Delta_2 - \frac{\Delta_1}{2}\right)\eta^2 n_2 + \epsilon_f n_H + e\phi(p - n_1 - n_2) + q\phi n_H \\ & + k_B T\left[p\ln\left(\frac{p}{N_v}\right) + (N_v - p)\ln\left(1 - \frac{p}{N_v}\right) + n_1\ln\left(\frac{n_1}{N_1}\right) + n_H\ln\left(\frac{n_H}{N_1}\right)\right. \\ & \left. + (N_1 - n_1 - n_H)\ln\left(1 - \frac{n_1 + n_H}{N_1}\right) + n_2\ln\left(\frac{n_2}{N_2}\right) + (N_2 - n_2)\ln\left(1 - \frac{n_2}{N_2}\right)\right], \end{aligned} \quad (2)$$

where the last two lines are the entropy contributions. ϵ_f is the formation energy of an interstitial hydrogen and ϕ is the electric potential. k_B is the Boltzmann constant, and T is the temperature. N_v, N_1, and N_2 are the effective densities of states of the valence band, the intermediate band, and the upper Hubbard band, respectively. Note that Eq. (2) does not depend on the microscopic origin of electron localization, which is probably complex and different in different materials. Therefore, our phase-field model is robust and general.

The resistance trees can be generated simply by applying a series of brief voltage pulses to the nickelate. The Joule heating power in the nickelate would be low because the nickelate remains an insulator during the whole process. Therefore, the temperature of the nickelate can be assumed to stay the same as the ambient temperature. This assumption also allows us to test whether the resistance states can be generated only by athermal effects. The equations of evolution for a general three-dimensional system are

$$\frac{\delta F}{\delta \eta} = 0, \qquad \frac{\delta F}{\delta S_1} = 0, \qquad \frac{\delta F}{\delta S_2} = 0, \quad (3)$$

TABLE I. Values of the parameters for $SmNiO_3$. κ_1 and κ_2 are typical values and K corresponds to a typical carrier lifetime of 1 ns. They all have minor effects on the simulation results [23]. M_h and M_e are on the typical order of magnitude at room temperature measured by experiments [46,47]. Δ_1 and Δ_2 correspond to a typical band gap of 0.1 eV at room temperature [2,48] and a Mott-Hubbard gap of 3 eV at zero temperature [4] of pristine $SmNiO_3$, respectively. N_v and N_1 correspond to one filled and one empty ligand oxygen hole per formula unit (f.u.), respectively [23,49]. N_2 is obtained by integrating the first-principles calculated density of states [4]. ϵ_f, ν, and a are adopted from this work [17]. $G^\ddagger$ corresponds to a proton diffusion coefficient of 1.6×10^{-7} cm^2/s measured at room temperature [50,51] and is close to the first-principles calculation results [17,52] indicating an intra-octahedral hopping mechanism for proton migration [52]. ε_r is the squared refractive index measured for hydrogenated $SmNiO_3$ [2,53].

κ_1	κ_2	Δ_1	Δ_2	ϵ_f	q	N_v	N_1
1 eV/nm	1 eV/nm	9.6 eV	16 eV	0.9 eV	$0.13e$	1 f.u.$^{-1}$	1 f.u.$^{-1}$
N_2	M_h	M_e	K	ν	a	$G^\ddagger$	ε_r
0.85 f.u.$^{-1}$	0.1 $cm^2/(s\,V)$	0.1 $cm^2/(s\,V)$	3.9 f.u./ns	782 GHz	0.435 nm	0.235 eV	4.8

$$\frac{\partial p}{\partial t} = \nabla \cdot \left(\frac{M_h}{e} p \nabla \frac{\delta F}{\delta p} \right) + K(\bar{p}\,\bar{n} - pn), \tag{4}$$

$$\frac{\partial n}{\partial t} = \nabla \cdot \left(\frac{M_e}{e} n \nabla \mu_e \right) + K(\bar{p}\,\bar{n} - pn), \tag{5}$$

$$\frac{\partial n_H}{\partial t} = \nabla \cdot \left[n_H \nu a e^{-G^\ddagger/(k_B T)} 2 \sinh \left(\frac{a}{2 k_B T} \nabla \frac{\delta F}{\delta n_H} \right) \right], \tag{6}$$

$$-\nabla^2 \phi = \frac{e(p-n)}{\varepsilon_r \varepsilon_0}, \tag{7}$$

where $\mu_e = \delta F/\delta n_1 = \delta F/\delta n_2$ and $n = n_1 + n_2$ [23]. $\bar{p}$ and $\bar{n}$ are the equilibrium densities of free holes and free electrons, respectively. K is a rate constant of electron-hole recombination. M_h and M_e are the mobilities of free holes and free electrons, respectively. We used the nonlinear transport theory for the proton migration [54], Eq. (6), where ν is the attempting frequency, a the hopping distance, and $G^\ddagger$ the hopping barrier. $\sinh(\cdot)$ of a vector means applying $\sinh(\cdot)$ to each component of the vector. ε_r is the dielectric constant of the hydrogenated nickelate taking into account bound charges from doped hydrogen atoms, and ε_0 is the vacuum permittivity.

The values of all the parameters are listed in Table I. There is only one fitting parameter, q, whose value is chosen for the simulated neural tree to best match the one obtained experimentally. To justify the choice of the value for q, we perform first-principles calculations of the Born effective charge (not totally equivalent to q) of a hydrogen atom in $H - SmNiO_3$, and find that it can be as low as $0.29e$ along some directions [23].

A one-dimensional system is adequate for simulating the trees because the expected highly resistive barrier should not form a filament, but should be approximately homogeneous along the direction perpendicular to the applied electric field [55]. The simulation details are described in Supplemental Material [23].

We first demonstrate in Fig. 2, upper panel that hydrogen doping increases the resistance R by more than 5 orders of magnitude, which agrees remarkably well with the experiment [9] and is a signature of the antidoping effect. The n_H dependence of the resistance is exponential only in the medium doping range $0.3\ \text{f.u.}^{-1} \lesssim n_H \lesssim 0.7\ \text{f.u.}^{-1}$. The gap also increases with increasing n_H and varies with n_H approximately linearly for $n_H \gtrsim 0.3\ \text{f.u.}^{-1}$. The steep increase in the resistance near $n_H = 0$ stems from the fast increase in the smaller gap E_{g1} as a function of n_H, whereas the steep increase in the resistance near $n_H = 1\ \text{f.u.}^{-1}$ is due to the saturating effect $R \sim (N_1 - n_H)^{-1}$.

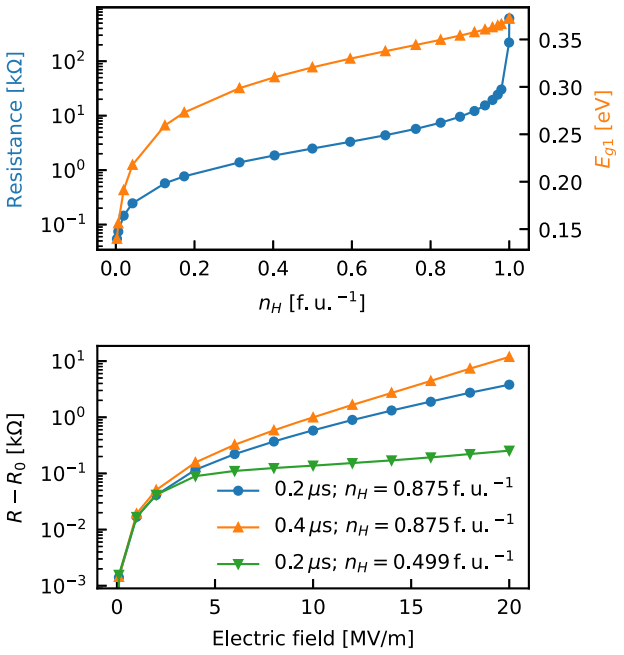

FIG. 2. Upper panel: resistance (R) and the smaller gap as functions of the homogeneous concentration of protons at zero electric field. Lower panel: resistance change as a function of the applied electric field with two different durations and of two different proton concentrations (the initial state is that of a homogeneous distribution of protons). R_0 is R at zero electric field. R is calculated by V/I, where V is the applied voltage and I is the boundary current obtained in the simulations.

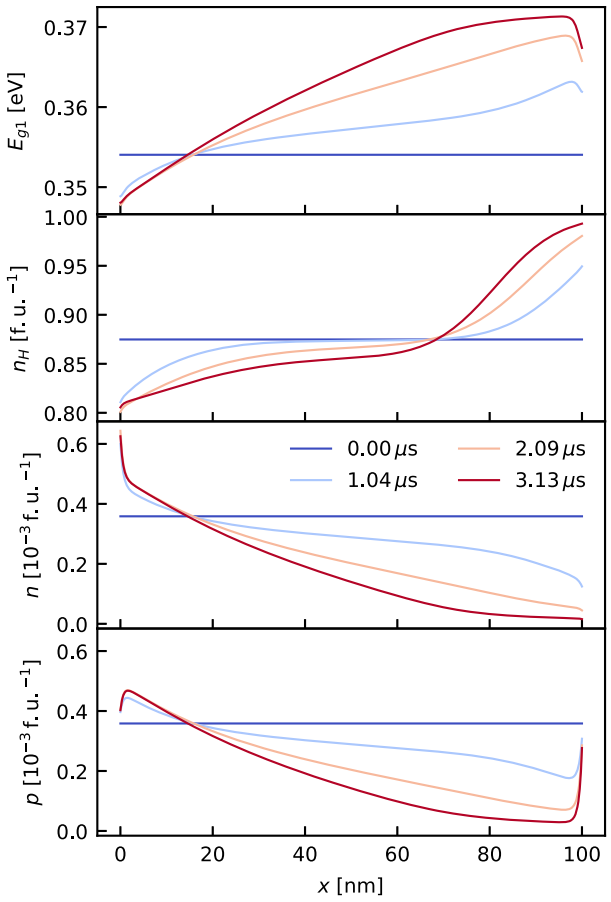

FIG. 3. Spatiotemporal evolution of the smaller gap E_{g1}, proton concentration n_H, free electron density n, and free hole density p at an electric field of 10 MV/m.

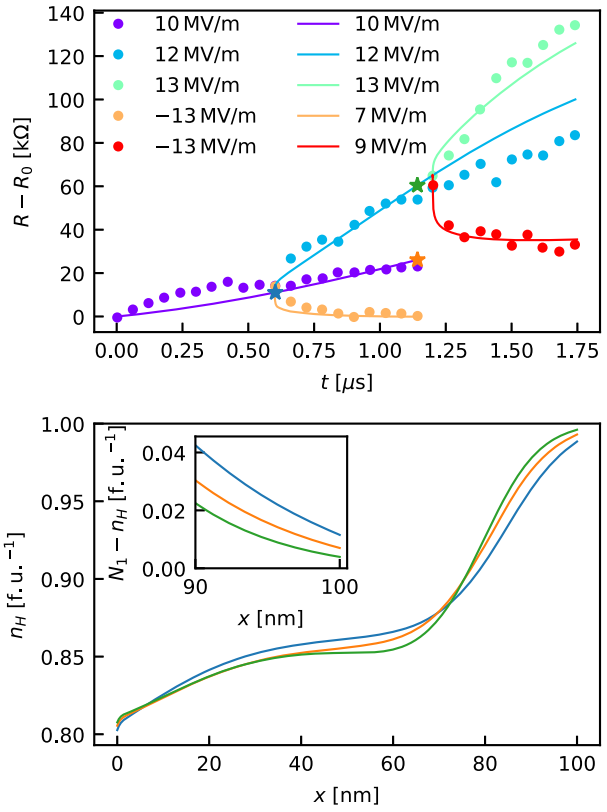

FIG. 4. Upper panel: comparison of experimentally measured (dots) and calculated neural trees, i.e., the resistance change as a function of time and applied electric field (see the legend). R_0 is the resistance at $t = 0$. Lower panel: proton concentration fields in the states marked by stars with the corresponding colors in the upper panel. The inset shows the corresponding densities of itinerant states on the ligand hole band.

We then show in Fig. 2, lower panel that the resistance increases with increasing electric field and that the resistance change for moderate electric fields ($\gtrsim$8 MV/m) depends on the field exponentially. This behavior remains the same as n_H is varied. If the electric field is applied for a longer time, the resistance increases further. These results are consistent with the experimental measurement for hydrogenated $NdNiO_3$ [17], whose resistance change behavior induced by hydrogenation is qualitatively the same as $SmNiO_3$ [7,14,15].

To see what happens during the voltage-induced resistance enhancement, we show in Fig. 3 the spatiotemporal evolution of various fields. Protons migrate from the left electrode, which is connected to the ground, to the right electrode with a negative voltage. This causes the free carrier density to decrease near the right electrode and increase near the left electrode with time, making the band gap increase near the right electrode and decrease near the left electrode. These result in a high-resistivity barrier near the right electrode, thus increasing the overall resistance of the sample. At $t = 3.13$ μs, within about 3 nm to the electrodes, p exhibits sharp spatial changes, which correspond to an accumulation of net charges due to the applied voltage. The band gap thereby drops in the vicinity of the right electrode due to the excess screening of electron-electron interaction there.

We finally depict in Fig. 4 the calculated resistance states as a function of time and the applied electric field. The simulation result is in excellent quantitative agreement with the experiment [17]. The small value of q that leads to this agreement is a strong indication of the unusual properties of antidoping and is a manifestation of strong electron localization and correlation. There are two points to be noted. One is that the initial proton concentration corresponding to the resistance R_0 in the experiment is not homogeneous, but higher near the negative (right) electrode and lower near the ground (left) electrode [17]. To account for this, we apply an electric field of 10 MV/m to the homogeneous initial state in Fig. 3 for 2 μs and take this state as the initial state ($t = 0$) for the simulation in Fig. 4. The other is that in the experiment every resistance state and thus the proton distribution are nonvolatile after the voltage is removed [17]. Therefore, to generate the two downward branches (orange and red dots in Fig. 4) of the tree, a bias of opposite polarity was applied to reverse the

proton distribution [17]. However, this is not the case in our model. As shown by Eq. (6), we model the evolution of the proton distribution using the canonical diffusion equation, so the proton distribution will return to the homogeneous state with a uniform chemical potential after we remove the voltage. As a result, we only need to apply a small positive electric field and then the proton distribution will be reversed slightly, thereby generating the downward branches (orange and red lines in Fig. 4). If one accounts for the nonvolatility by holding the previously applied voltage, the electric fields generating the two downward branches would be the same ($7\ \mathrm{MV/m} - 10\ \mathrm{MV/m} = 9\ \mathrm{MV/m} - 12\ \mathrm{MV/m}$), consistent with the experiment.

The mechanism of this nonvolatility of the proton distribution is currently not known; it is possibly related to multiple stable interstitial positions for protons resembling the property of spin glasses and the concentration-dependent formation energy of interstitial protons [12]. It is thus currently not feasible to incorporate the nonvolatility into the phase-field model and should be a subject of future study.

The lower panel of Fig. 4 shows the proton distribution in the states marked by stars in the upper panel. For a constant electric field, n_H at different times roughly intersect at the same point as shown in Fig. 3. In contrast, the intersection point of the green-star n_H and the blue-star reference n_H moves 2.7 nm to the right compared to that of the orange-star n_H and the reference n_H. Meanwhile, in a large portion of the $x \gtrsim 60$ nm range, the deviation of the green-star n_H from the reference n_H is nearly twice that of the orange-star n_H from the reference n_H. Because of this proton redistribution, as the state goes from the orange star to the green star, the density of *itinerant* states on the ligand hole band, $N_1 - n_H$, in the $90 \leq x \leq 100$ nm range decreases by about 30%–50% (inset in Fig. 4), leading to greater blockage of current near the right electrode. Therefore, although the branches of the tree are saturating, i.e., their slopes decrease with time, a higher electric field can generate a new branch by reactivating the proton redistribution process. Since we presumed the isothermal condition, our results demonstrate that the resistance trees can be generated in an athermal manner. If q is anisotropic, the saturating speed of the branches will be different as the electric field is applied in different directions to a three-dimensional system.

In conclusion, we derived a phase-field model of anti-doping based on its microscopic mechanism and used it to unambiguously demonstrate that the perovskite neural trees are generated by the voltage-induced reactivation of proton redistribution. Our model can be further improved to incorporate the nonvolatility of the proton distribution. The results are of broad relevance to understanding the origin of memory formation in quantum materials and metastable matter that are of interest to emerging information processing technologies. The model is general, and one could incorporate material-specific parameters to model other materials with different dopants.

This work was supported as part of the Computational Materials Sciences Program funded by the U.S. Department of Energy, Office of Science, Basic Energy Sciences, under Award No. DE-SC0020145 (Y. S., G. D. Z., I .D., and L. Q. C.). The first-principles calculations by G. D. Z. were also partially supported by the Hamer Foundation through the Hamer Professorship at the Pennsylvania State University. S. R. acknowledges AFOSR FA9550-22-1-0344 for support.

*yxs187@psu.edu
†lqc3@psu.edu

[1] M. Imada, A. Fujimori, and Y. Tokura, Metal-insulator transitions, Rev. Mod. Phys. **70**, 1039 (1998).
[2] J. Shi, Y. Zhou, and S. Ramanathan, Colossal resistance switching and band gap modulation in a perovskite nickelate by electron doping, Nat. Commun. **5**, 4860 (2014).
[3] N. Lu, P. Zhang, Q. Zhang, R. Qiao, Q. He, H.-B. Li, Y. Wang, J. Guo, D. Zhang, Z. Duan, Z. Li, M. Wang, S. Yang, M. Yan, E. Arenholz, S. Zhou, W. Yang, L. Gu, C.-W. Nan, J. Wu, Y. Tokura, and P. Yu, Electric-field control of tri-state phase transformation with a selective dual-ion switch, Nature (London) **546**, 124 (2017).
[4] Q. Liu, G. M. Dalpian, and A. Zunger, Antidoping in insulators and semiconductors having intermediate bands with trapped carriers, Phys. Rev. Lett. **122**, 106403 (2019).
[5] O. I. Malyi and A. Zunger, Hole antidoping of oxides, Phys. Rev. B **101**, 235202 (2020).
[6] A. Zunger and O. I. Malyi, Understanding doping of quantum materials, Chem. Rev. **121**, 3031 (2021).
[7] J. Chen, Y. Zhou, S. Middey, J. Jiang, N. Chen, L. Chen, X. Shi, M. Döbeli, J. Shi, J. Chakhalian, and S. Ramanathan, Self-limited kinetics of electron doping in correlated oxides, Appl. Phys. Lett. **107**, 031905 (2015).
[8] C. Oh, S. Heo, H. M. Jang, and J. Son, Correlated memory resistor in epitaxial $NdNiO_3$ heterostructures with asymmetrical proton concentration, Appl. Phys. Lett. **108**, 122106 (2016).
[9] K. Ramadoss, F. Zuo, Y. Sun, Z. Zhang, J. Lin, U. Bhaskar, S. Shin, M. A. Alam, S. Guha, D. Weinstein, and S. Ramanathan, Proton-doped strongly correlated perovskite nickelate memory devices, IEEE Electron Device Lett. **39**, 1500 (2018).
[10] C. Oh, M. Jo, and J. Son, All-solid-state synaptic transistors with high-temperature stability using proton pump gating of strongly correlated materials, ACS Appl. Mater. Interfaces **11**, 15733 (2019).
[11] I. Matsuzawa, T. Ozawa, Y. Nishiya, U. Sidik, A. N. Hattori, H. Tanaka, and K. Fukutani, Controlling dual mott states by hydrogen doping to perovskite rare-earth nickelates, Phys. Rev. Mater. **7**, 085003 (2023).
[12] K. Yamauchi and I. Hamada, Hydrogen-induced insulating state accompanied by interlayer charge ordering in $SmNiO_3$, Phys. Rev. B **108**, 045108 (2023).

[13] X. Gao, J. Liu, Y. Ji, L. Wei, W. Xiao, S. Hu, L. Li, K. Chen, and Z. Liao, Giant resistive switching and lattice modulation at full temperature range in a Sr-doped nickelate oxide transistor, Adv. Electron. Mater. **9**, 2300116 (2023).

[14] Y. Bian, H. Li, F. Yan, H. Li, J. Wang, H. Zhang, Y. Jiang, N. Chen, and J. Chen, Hydrogen induced electronic transition within correlated perovskite nickelates with heavy rare-earth composition, Appl. Phys. Lett. **120**, 092103 (2022).

[15] H. Li, Y. Li, B. Li, W. Huang, and Y. Ding, Preparation of $ReNiO_3$ $(Re = Pr, Sm, Eu)$ and proton conductivity, RSC Adv. **14**, 147 (2024).

[16] M. Kotiuga and K. M. Rabe, High-density electron doping of $SmNiO_3$ from first principles, Phys. Rev. Mater. **3**, 115002 (2019).

[17] H.-T. Zhang *et al.*, Perovskite neural trees, Nat. Commun. **11**, 2245 (2020).

[18] R. S. Bisht *et al.*, Spatial interactions in hydrogenated perovskite nickelate synaptic networks, Nano Lett. **23**, 7166 (2023).

[19] D. Kawamoto, A. N. Hattori, M. Yamamoto, X. L. Tan, K. Hattori, H. Daimon, and H. Tanaka, Correlation between Ni valence and resistance modulation on a $SmNiO_3$ chemical transistor, ACS Appl. Electron. Mater. **1**, 82 (2019).

[20] Y. Shi and L.-Q. Chen, Current-driven insulator-to-metal transition in strongly correlated Vo_2, Phys. Rev. Appl. **11**, 014059 (2019).

[21] Y. Shi, V. Gopalan, and L.-Q. Chen, Phase-field model of coupled insulator-metal transitions and oxygen vacancy redox reactions, Phys. Rev. B **107**, L201110 (2023).

[22] Y. Shi and L.-Q. Chen, Sublattice-dependent antiferromagnetic transitions in rare earth nickelates, Phys. Rev. Lett. **130**, 186801 (2023).

[23] See Supplemental Material at http://link.aps.org/supplemental/10.1103/PhysRevLett.132.256502 for the details of the first-principles calculations and phase-field simulations, which includes Refs. [24–44].

[24] G. Giovannetti, S. Kumar, D. Khomskii, S. Picozzi, and J. van den Brink, Multiferroicity in rare-earth nickelates $RnIo_3$, Phys. Rev. Lett. **103**, 156401 (2009).

[25] A. Hampel and C. Ederer, Interplay between breathing mode distortion and magnetic order in rare-earth nickelates $R\ NiO_3$ within DFT + U, Phys. Rev. B **96**, 165130 (2017).

[26] A. Hampel, P. Liu, C. Franchini, and C. Ederer, Energetics of the coupled electronic–structural transition in the rare-earth nickelates, npj Quantum Mater. **4**, 5 (2019).

[27] G. Henkelman, A. Arnaldsson, and H. Jónsson, A fast and robust algorithm for bader decomposition of charge density, Comput. Mater. Sci. **36**, 354 (2006).

[28] J. Heyd, G. E. Scuseria, and M. Ernzerhof, Hybrid functionals based on a screened coulomb potential, J. Chem. Phys. **118**, 8207 (2003).

[29] J. Heyd, G. E. Scuseria, and M. Ernzerhof, Erratum: Hybrid functionals based on a screened coulomb potential, J. Chem. Phys. **124**, 219906(E) (2006).

[30] G. Kresse and J. Furthmüller, Efficiency of ab-initio total energy calculations for metals and semiconductors using a plane-wave basis set, Comput. Mater. Sci. **6**, 15 (1996).

[31] G. Kresse and J. Furthmüller, Efficient iterative schemes for ab initio total-energy calculations using a plane-wave basis set, Phys. Rev. B **54**, 11169 (1996).

[32] A. I. Liechtenstein, V. I. Anisimov, and J. Zaanen, Density-functional theory and strong interactions: Orbital ordering in Mott-Hubbard insulators, Phys. Rev. B **52**, R5467 (1995).

[33] A. Mercy, J. Bieder, J. Íñiguez, and P. Ghosez, Structurally triggered metal-insulator transition in rare-earth nickelates, Nat. Commun. **8**, 1677 (2017).

[34] J. P. Perdew, A. Ruzsinszky, G. I. Csonka, O. A. Vydrov, G. E. Scuseria, L. A. Constantin, X. Zhou, and K. Burke, Restoring the density-gradient expansion for exchange in solids and surfaces, Phys. Rev. Lett. **100**, 136406 (2008).

[35] J. P. Perdew, K. Burke, and M. Ernzerhof, Generalized gradient approximation made simple, Phys. Rev. Lett. **77**, 3865 (1996).

[36] E. Sanville, S. D. Kenny, R. Smith, and G. Henkelman, Improved grid-based algorithm for Bader charge allocation, J. Comput. Chem. **28**, 899 (2007).

[37] W. Tang, E. Sanville, and G. Henkelman, A grid-based Bader analysis algorithm without lattice bias, J. Phys. Condens. Matter **21**, 084204 (2009).

[38] J. Varignon, M. N. Grisolia, J. Íñiguez, A. Barthélémy, and M. Bibes, Complete phase diagram of rare-earth nickelates from first-principles, npj Quantum Mater. **2**, 21 (2017).

[39] P. Yoo and P. Liao, Metal-to-insulator transition in $SmNiO_3$ induced by chemical doping: A first principles study, Mol. Syst. Design Eng. **3**, 264 (2018).

[40] M. Yu and D. R. Trinkle, Accurate and efficient algorithm for Bader charge integration, J. Chem. Phys. **134**, 064111 (2011).

[41] I. A. Baratta, J. P. Dean, J. S. Dokken, M. Habera, J. S. Hale, C. N. Richardson, M. E. Rognes, M. W. Scroggs, N. Sime, and G. N. Wells, DOLFINx: The next generation FEniCS problem solving environment, preprint (2023), 10.5281/zenodo.10447666.

[42] M. S. Alnaes, A. Logg, K. B. Ølgaard, M. E. Rognes, and G. N. Wells, Unified form language: A domain-specific language for weak formulations of partial differential equations, ACM Trans. Math. Softw. **40**, 1 (2014).

[43] M. W. Scroggs, I. A. Baratta, C. N. Richardson, and G. N. Wells, Basix: A runtime finite element basis evaluation library, J. Open Source Software **7**, 3982 (2022).

[44] M. W. Scroggs, J. S. Dokken, C. N. Richardson, and G. N. Wells, Construction of arbitrary order finite element degree-of-freedom maps on polygonal and polyhedral cell meshes, ACM Trans. Math. Softw. **48**, 1 (2022).

[45] D. Kavetski, P. Binning, and S. W. Sloan, Adaptive backward Euler time stepping with truncation error control for numerical modelling of unsaturated fluid flow, Int. J. Numer. Methods Eng. **53**, 1301 (2002).

[46] S. D. Ha, R. Jaramillo, D. M. Silevitch, F. Schoofs, K. Kerman, J. D. Baniecki, and S. Ramanathan, Hall effect measurements on epitaxial $SmNiO_3$ thin films and implications for antiferromagnetism, Phys. Rev. B **87**, 125150 (2013).

[47] J. Shamblin, M. Heres, H. Zhou, J. Sangoro, M. Lang, J. Neuefeind, J. A. Alonso, and S. Johnston, Experimental evidence for bipolaron condensation as a mechanism for the metal-insulator transition in rare-earth nickelates, Nat. Commun. **9**, 86 (2018).

[48] M. L. Medarde, Structural, magnetic and electronic properties of perovskites (r = rare earth), J. Phys. Condens. Matter **9**, 1679 (1997).
[49] S. Catalano, M. Gibert, J. Fowlie, J. Íñiguez, J. M. Triscone, and J. Kreisel, Rare-earth nickelates $RnIo_3$: Thin films and heterostructures, Rep. Prog. Phys. **81**, 046501 (2018).
[50] Y. Zhou, X. Guan, H. Zhou, K. Ramadoss, S. Adam, H. Liu, S. Lee, J. Shi, M. Tsuchiya, D. D. Fong, and S. Ramanathan, Strongly correlated perovskite fuel cells, Nature (London) **534**, 231 (2016).
[51] Y. Taniguchi, H.-B. Li, A. N. Hattori, and H. Tanaka, Comprehensive determination of proton diffusion in protonated $NdNiO_3$ thin film by a combination of electrochemical impedance spectroscopy and optical observation, Appl. Phys. Express **16**, 035501 (2023).
[52] C. Lan, H. Li, and S. Zhao, A first-principles study of the proton and oxygen migration behavior in the rare-earth perovskite $SmNiO_3$, J. Comput. Electron. **19**, 905 (2020).
[53] Z. Zhang *et al.*, Perovskite nickelates as electric-field sensors in salt water, Nature (London) **553**, 68 (2018).
[54] N. F. Mott and R. W. Gurney, *Electronic Processes in Ionic Crystals* (Oxford Clarendon Press, Oxford, 1948).
[55] I. A. Zaluzhnyy, P. O. Sprau, R. Tran, Q. Wang, H.-T. Zhang, Z. Zhang, T. J. Park, N. Hua, B. Stoychev, M. J. Cherukara, M. V. Holt, E. Nazaretski, X. Huang, H. Yan, A. Pattammattel, Y. S. Chu, S. P. Ong, S. Ramanathan, O. G. Shpyrko, and A. Frano, Proton distribution visualization in perovskite nickelate devices utilizing nanofocused x rays, Phys. Rev. Mater. **5**, 095003 (2021).

Correction: A missing term in Eq. (6) has been inserted.